ROYAL SOCIETY OF CHEMISTRY

PAPER

Check for updates

Understanding charge separation in CdS/Ce-UiO66-NH$_2$ heterojunctions for enhanced photocatalytic hydrogen evolution†‡

Wenqing Hou, [ID] [ab] Sam A. J. Hillman, [ID] [a] Soranyel Gonzalez-Carrero, [ID] [ad] Shilin Yao, [a] Huangtianzhi Zhu[c] and James R. Durrant [ID] *[a]

UiO metal–organic frameworks (MOFs) are regarded as promising photocatalysts due to their unique stability and band designability. We recently demonstrated that the cerium-based Ce-UiO-NH$_2$ exhibited an enhanced hydrogen evolution relative to zirconium (Zr)-UiOs, when loaded with cadmium sulfide (CdS). However, the underlying charge separation dynamics of this system is unclear. In this work, we optimised the CdS loading and used transient absorption and electrochemical spectroscopy to investigate the charge separation dynamics and energetics in the CdS/Ce-UiO-NH$_2$ heterojunction. The optimised heterojunction showed improved stability and achieved an external quantum efficiency (EQE) of 2.2% under 420 nm LED illumination whilst using methanol as a sacrificial agent. The heterojunction facilitates charge separation, generating long-lived (ms) holes on Ce-UiO-NH$_2$ and electrons on the CdS. In contrast with electron-accepting Zr-UiOs, this study reveals a reversed charge separation direction in CdS/UiO heterojunctions with Ce-UiO-NH$_2$ acting as the electron donor.

Introduction

In recent years, the world's energy shortage and environmental pollution have become urgent issues. It is therefore imperative to seek new technologies to relieve these pressures. Among them, photocatalytic hydrogen (H$_2$) evolution from water under solar light irradiation is regarded as a promising clean energy technology and has developed rapidly in recent years.[1,2] In particular, research has focused on exploring new, more efficient materials and heterojunctions and has achieved significant progress.[3,4] Meanwhile, understanding such materials' underlying reaction mechanisms is attracting increasing attention, and is playing a significant role in the design of efficient photocatalysts.

Among various photocatalysts, MOFs have received significant attention owing to their high surface areas, visible-light-response, and tunable functional structure.[5] The large

[a]Department of Chemistry and Centre for Processable Electronics, Imperial College London, White City Campus, London W12 0BZ, UK. E-mail: j.durrant@imperial.ac.uk

[b]State Key Laboratory of Silicon Materials and Department of Chemistry, Zhejiang University, Hangzhou 310027, China

[c]Yusuf Hamied Department of Chemistry, University of Cambridge, Lensfield Road, Cambridge CB2 1EW, UK

[d]Institute of Molecular Science, University of Valencia, Paterna, Valencia 46980, Spain

number of possible combinations of constituent metal clusters and bridging organic linkers offer considerable synthetic flexibility when targeting superior visible-light-driven photocatalysis.[6,7] It has been demonstrated that MOFs can show charge transfer from the organic linkers to the metal nodes (*i.e.* linker-to-metal transfer) which is triggered by light irradiation.[8] As such, they can act as semiconductor photocatalysts which absorb light, generate electron/hole pairs, and then initiate either the hydrogen evolution reaction (HER) or the oxygen evolution reaction (OER).

UiO-66s (Universite i Oslo) are amongst the most important MOFs and have gained intensive attention due to their thermal and chemical stabilities and facile design.[9,10] Ce-UiO-NH$_2$ is an analogue of the Zr-UiO, comprising hexanuclear clusters constituted by cerium-oxo [Ce$_6$(O)$_4$(OH)$_4^{12+}$] and 2-amino-terephthalic acid.[11,12] With Ce metal node substitution, it is possible to achieve better visible light absorption and catalytic properties due to the Ce(III)/(IV) redox properties (Ce(III)/(IV) couple at circa 1.61 V *vs.* NHE) and the presence of low energy 4f orbitals.[13] However, UiO-66 in isolation only shows minimal photocatalytic activity. Significant efforts have been made to improve their photocatalytic HER efficiency through methods such as loading noble metal co-catalysts (Pt, Au),[14,15] using amino-substituted organic linkers to increase the visible light photoresponse,[16] or combining with conventional semiconductors in a heterojunction.[17] Heterojunction design is considered as one of the most promising strategies due to its potential for improved charge separation and the advantages of combining different catalysts. Cadmium sulfide (CdS)

nanoparticles are considered to be a good junction material for MOFs due to its strong visible light absorption (optical band gap 2.3 eV). However, its function can be seriously limited by self-corrosion and the rapid recombination of photogenerated electrons and holes.[18,19] In 2015, Shen and co-workers reported CdS/UiO-66 composites decorated with MoS_2 for enhanced HER. Jiang's group studied the dynamics of CdS/UiO-66 composites for enhanced HER in 2018, indicating the potential of UiO-66 working as an electron acceptor.[17,20]

In our previous work, UiO-66s were compared as supports for CdS nanoparticles (NPs) to enhance HER efficiency under visible light in sodium sulfide/sodium sulfite (Na_2S/Na_2SO_3) aqueous solution.[21] The maximum EQE was obtained using a Ce-substituted UiO-NH_2. Spectral and electrochemical measurements indicated that Ce-UiO-NH_2 is a more efficient partner with CdS due to its smaller band gap and more efficient charge transfer to CdS. However, the underlying charge dynamics of CdS/Ce-UiO-NH_2 have not previously been reported, and there is no direct evidence indicating whether Ce-UiO-NH_2 acts as electron donor or acceptor in this heterojunction. In the work herein, we improved the HER efficiency by optimizing the loading of CdS onto the Ce-UiO-NH_2 framework and using methanol as the sacrificial regent. The charge separation dynamics in the CdS/Ce-UiO-NH_2 heterojunction were then investigated by transient absorption spectroscopy. The optimized heterojunction was found to exhibit a much higher density of long-lived (ms) charges, consistent with its enhanced photocatalytic efficiency. Furthermore, the direction of charge transfer direction was studied using transient absorption spectroscopy and spectroelectrochemistry, determining the role of Ce-UiO-NH_2 as the electron donor in this heterojunction.

Experimental

Materials preparation

Chemicals were in analytic grade and were used without further purification. Terephthalic acid (BDC, 99%), $Ce(NH_4)_2(NO_3)_6$, $Cd(CH_3COO)_2$, Na_2S, acetonitrile (ACN) and *N*,*N*-dimethylformamide (DMF) were from Sigma-Aldrich. 2-Aminoterephthalic acid (ATA, 98%) were purchased from Thermo Scientific Chemicals. Catalysts were synthesized according to the previous work.[21] Ce-UiO-NH_2: Ce-UiO-NH_2 was prepared by solvent-assistant-linker-exchange procedure.[12] Ce-UiO66 (Ce-UiO) was firstly prepared as follows,[11] terephthalic acid (143 mg, 0.86 mmol) was dissolved in 4.9 mL of DMF. After that, 1.6 mL of a 0.535 M aqueous solution of $Ce(NH_4)_2(NO_2)_6$ was added and the mixture was heated at 100 °C under stirring conditions for 15 min. Then, the precipitate was collected by centrifugation and purified three times with DMF and acetone respectively to remove the residue of organic ligands and DMF. The final product was dried overnight (60 °C). Second, for synthesis of Ce-UiO-NH_2, Ce-UiO (81.6 mg, 0.25 mmol) and ATA (181.1 mg, 1 mmol) were dispersed in methanol (25 mL). The mixture was stirred for dissolving completely and then sonicated for 5 min, followed by purifying with DMF and ethanol, respectively. The final product was collected by centrifugation and dried under vacuum (60 °C, 12 h). *x*CdS/Ce-UiO-NH_2: neat

CdS NPs and 20–50 wt%CdS/Ce-UiO-NH_2 (20–50%CdS/Ce-UiO-NH_2 for short), were prepared by two-step-loading following the recipe in Table S1.† Typically, Ce-UiO-NH_2 (60 mg) was activated under vacuum (40 °C, 12 h) and dispersed in 15 mL DI water. Afterwards, $Cd(CH_3COO)_2$ aqueous solution (2 mL, 103.8 M) was dropwise added into the solution with stirring for 2 h, and then with Na_2S (2 mL, 103.8 M). After stirring for 5 h continuously, the product (40% CdS/Ce-UiO-NH_2) was collected by centrifugation, purified with DI water and ethanol and dried under vacuum (60 °C, 12 h).

Materials characterizations

Powder X-ray diffraction pattern (XRD) was obtained on a Rigaku diffractometer with Cu Kα as X-ray. The absorption spectra were recorded in an Agilent Cary 5000 UV-visible NIR spectrometer. The high-resolution transmission electron microscopic images (HRTEM) were taken by JEM-2100F at 150 kV accelerating voltage. Fourier transform infrared microscopy (FTIR) was collected using a Cary 630 FT-IR spectrometer in the wavenumber range 500–4000 cm^{-1}. The steady-state photoluminescence (PL) spectra were recorded using an Edinburgh FLS1000 photoluminescence spectrometer.

Hydrogen evolution

The photocatalytic H_2 evolution was measured using methanol as a sacrificial electron donor. In a 100 mL sealed flat bottom flask, 25 mg of catalyst were dispersed in 50 mL aqueous solution (methanol, 10 vol%). Before irradiation, the reactor was purged for 30 min with argon to remove the oxygen and stirred at room temperature with irradiated by four 3 W LED lamps (420 nm), located at 1.0 cm away from the solution surface. H_2 evolution was analyzed by gas chromatography (GC) equipped with a thermal conductivity detector (Agilent GC7820A). The stability test was performed with 40%CdS/Ce-UiO-NH_2, with 120 min of irradiation. After one run was complete, the system was purged with argon for 30 min and irradiated again, without extra addition of new catalyst and sacrificial reagent.

The EQE was measured under the same conditions as H_2 evolution measurements. The illumination intensity was measured by using a UV-A radiometer (0.1 J cm^{-2}, from Beijing Shida Technology Co., Ltd), and the EQE was calculated by the following equation:

$$EQE(\%) = \frac{\text{Number of evolved } H_2 \text{ molecules} \times 2}{\text{Number of incident photons}} \times 100$$

$$\text{Number of incident photons} = \frac{E_p}{h\nu}$$

where E_p is the total energy of incident photons (J), h is the Planck constant (J s^{-1}), ν is the frequency of light (Hz).

Transient absorption spectroscopy (TAS)

Microsecond to second TAS data were acquired on previously-described home-built setups.[22] 420 nm or 560 nm laser excitation was generated from a Nd:YAG laser (OPOTEK Opolette 355

II, 6 ns pulse width). The probe beam was generated from a quartz halogen lamp. The light was directed through the sample to a monochromator, which selected the probe wavelength and was relayed to a Si photodiode detector (Hamamatsu S1722-01). Data on the sub-ms timescale were amplified with an electronic amplifier box (Costronics 2011 amplifier) and recorded on an oscilloscope (Tektronix DPO 3012). Data on the ms timescale were simultaneously recorded on a National Instruments DAQ card (National Instruments USB-6361). Pulse energies were measured by energy meter (OPHIR Photonics, VEGA P/N 7Z01560). Film samples were made by drop casting on FTO glass with acetonitrile (ACN) suspension (2 mg catalysts, 20 μL Nafion and 400 μL ACN). Films were measured in DI water or aqueous solution and purged with argon to remove oxygen. To ensure equal numbers of absorbed photons, all films were deposited such that they had the same ground state absorbance at the excitation wavelength (absorbance = 0.6 at 420 nm excitation and absorbance = 0.25 at 560 nm excitation).

Electrochemical spectroscopy

Electrochemical measurements were conducted using a three-electrode setup with $NaClO_4$ electrolyte (pH 7), sample as working electrode, Pt wire counter electrode, and an Ag/AgCl reference electrode (saturated KCl). A PGSTAT204 potentiostat (Metrohm-Autolab, The Netherlands) was used to apply linear sweep voltammograms with potential steps of 50 mV at rate of 50 mV s^{-1}. Absorbance changes from 400–1000 nm were collected at each applied potential with a Maya2000Pro spectrometer (OceanOptics) using home-built LabView software (https://opensourcespectroscopy.com/sec_code/). All measurements were conducted on three separate batches of samples, to verify reproducibility and to calculate standard deviation. All potentials are presented against relative hydrogen electrode (RHE) through the following equation:

$$E\ (V\ vs.\ \text{RHE}) = E\ (V\ vs.\ \text{AgCl/Ag}) + 0.059 \times \text{pH} + 0.197$$

Results and discussion

Heterojunction design and characterization

CdS/Ce-UiO-NH$_2$ samples were synthesized in accordance with the protocol described in the previous work.[21] Ce-UiO-NH$_2$ was firstly synthesized by a solvothermal method followed by a solvent-assisted-linker-exchange procedure. Then CdS was loaded onto Ce-UiO-NH$_2$ frameworks using a two-step loading to form heterojunctions (Fig. 1a). The structure and composition of all materials were investigated by XRD, HRTEM, FTIR and N$_2$ sorption. According to powder XRD (Fig. 1d), Ce-UiO-NH$_2$ has similar topological structure to other UiO-66 MOFs,[10,11] showing the characteristic peaks at 7.20, 8.30, 11.70, 13.76, 16.52, 18.02, 21.28 and 24.86°, respectively. CdS had a XRD pattern in accord with that for cubic CdS. After CdS loading, the heterojunctions exhibited visible diffraction patterns of both components. The characteristic powder XRD pattern of CdS increased in intensity and the pattern of Ce-UiO-NH$_2$ decreased
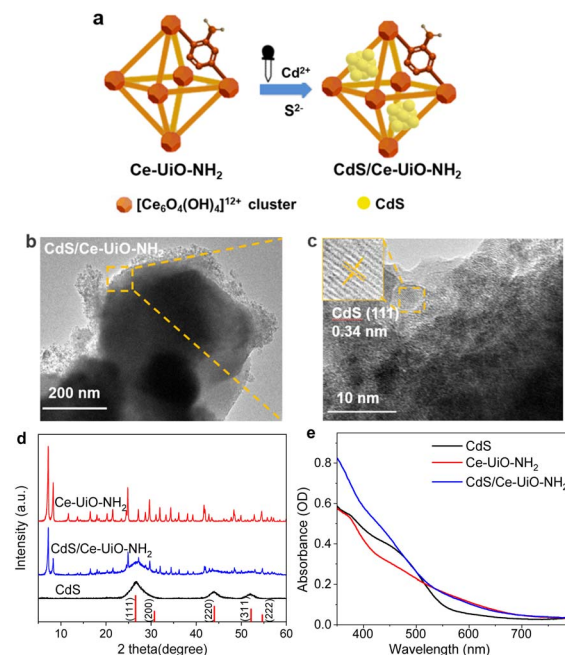

Fig. 1 (a) Synthesis of CdS/Ce-UiO-NH$_2$ heterojunctions, (b and c) HRTEM images for 40%CdS/Ce-UiO-NH$_2$, (d) XRD patterns and (e) absorption spectra for CdS, Ce-UiO-NH$_2$ and 40%CdS/Ce-UiO-NH$_2$, measured on film samples. The red columns represent the patterns for cubic CdS (JCPDS 80-0019).

in intensity as the CdS loading was increased (Fig. S1a†). In HRTEM images (Fig. 1b and c), small particles (5–10 nm) on large octahedrons (200–300 nm) were observed. The former had a distinct lattice spacing of 0.34 nm which matches well with the (111) facet of CdS, demonstrating that CdS NPs were evenly distributed on Ce-UiO-NH$_2$.

FTIR spectroscopy was conducted to investigate the organic structures inside Ce-UiO-NH$_2$. As shown in Fig. S1c,† some specific peaks of Ce-UiO-NH$_2$ were observed: at 1260 cm^{-1} (stretching vibration of C$_{ar}$–N); at 3500–3200 cm^{-1} (two stretching vibration N–H peaks caused by the amino groups); at 1650–1450 cm^{-1} (stretching vibrations caused by C=C); and at 1655 cm^{-1} (stretching vibrations of C=O). The lower frequency bonds at 800–450 cm^{-1} are attributed to the bending vibration of O–H and C–H, mixed with Ce–O bonds.[23]

N$_2$ sorption measurements were performed to evaluate the porosity of the heterojunctions. The results are shown in Table S2 and Fig. S1b.† The sorption isotherm of Ce-UiO-NH$_2$ shows the type I adsorption isotherm curve shape, whilst CdS exhibits type IV. The specific BET surface area (A_{sp}) of Ce-UiO-NH$_2$ was calculated to be 942 m^2 g^{-1}, with a large micropore volume (V_{mp}, 0.416 cm^3 g^{-1}) and total pore volume (V_{tp}, 0.521 cm^3 g^{-1}). With increasing content of CdS, the isotherm transitions from type I to type IV with increasing amounts of hysteresis. A_{sp}, V_{mp} and V_{tp} of the composites decreased, respectively. These changes are ascribed to the load of CdS on the Ce-UiO-NH$_2$. It is notable that the measured values were much smaller than those calculated from neat CdS and Ce-UiO-NH$_2$, whilst the ratio of V_{mp} to V_{tp} dramatically decreased from 0.80 to 0.32 as the CdS content increased from 0 to 50% (Table S2†). All these decreases

suggest that the CdS NPs are filling up the pores of Ce-UiO-NH$_2$ *via* the two-step loading procedure. Meanwhile, the reduced V_{mp} and increased pore size (d_p) with CdS loaded were also in agreement with the fact that the pore space of Ce-UiO-NH$_2$ was filled with CdS NPs.

Fig. 1e shows the steady state UV-vis absorption spectra. The spectrum of neat CdS NPs displays visible light absorption with an absorption edge at 550 nm (optical band gap: 2.25 eV), which can be attributed to the intrinsic band gap absorption of cubic CdS. For Ce-UiO-NH$_2$, there is a broad absorption tail that extends across the visible up to 700 nm. This absorption is clearly redshifted compared to Zr-based UiO66-NH$_2$ (450 nm) and is attributed to the narrower bandgap of Ce-UiO-NH$_2$. This is because the orbital energy of Ce 4f, which contributes to the lowest unoccupied linker orbitals, is lower than the Zr 4d orbital energy and exhibits more favorable linker-to-metal charge transfer in UiO-NH$_2$.[13] Meanwhile, the broad visible light absorption starting from 700 nm is suggestive of a complex band-to-band structure in Ce-UiO-NH$_2$. For CdS/Ce-UiO-NH$_2$, the absorbance spectrum combines the features of neat CdS and Ce-UiO-NH$_2$. These observations are in agreement with our previous work,[21] and confirm the successful and consistent synthesis of the neat and heterojunction materials.

Photocatalytic activity for hydrogen evolution

After determining the structure of CdS and Ce-UiO-NH$_2$ photocatalysts, their performance for H$_2$ evolution was measured under 420 nm LED excitation, using 10 vol% methanol aqueous solution as a hole scavenger. Fig. 2a shows the result of H$_2$ evolution on xCdS/Ce-UiO-NH$_2$ samples. The amount of H$_2$ evolved approximately linearly with time. We note that the H$_2$ evolved in the first 30 min was slightly lower than expected for linear H$_2$ evolution, likely due to the initial system heating. To assess the relative activity of those catalysts, the amount of H$_2$ evolved at 2 h and EQE were used as measure. Neat Ce-UiO-NH$_2$ showed negligible H$_2$ evolution within 2 h, whilst neat CdS also performed poorly. After loading with 20, 30, 40 and 50% CdS, however, the amount of H$_2$ evolution in 2 h increased to 60.2, 84.6, 103.2 and 89.9 μmol, respectively. The maximum EQE at 420 nm was 2.2%, observed at $x = 40\%$, which was 11.0 times

higher than the EQE of individual CdS (0.2%). It is worth noting that the 40%CdS/Ce-UiO-NH$_2$ heterojunction evolves hydrogen approximately 10 times more efficiently than Pt-loaded Ce-UiO-NH$_2$ (Table S3†). Further, the HER performance of the CdS/Ce-UiO-NH$_2$ was generally of similar order of magnitude to other reported CdS/MOFs. However, the vastly different experimental conditions used in the literature (sacrificial reagents, light intensity, *etc.*) prevent meaningful comparison.

Fig. 2b shows six successive 2 h tests for H$_2$ evolution. From the first run to the sixth, the amount of H$_2$ evolved decreased by only 3.75% for 40%CdS/Ce-UiO-NH$_2$ (from 102.17 μmol to 98.34 μmol) while the neat CdS decreased by 25.3% (from 9.43 μmol to 7.04 μmol, Fig. S2a†), demonstrating the improved HER stability of the heterojunction (marked as HJ for short). The stability of samples was further confirmed by XRD and XPS (Fig. S2†). For neat CdS, the diffraction peaks (such as those at $2\theta \approx 26.5°$, 44.0°, and 52.2° for CdS) decreased in intensity after hydrogen evolution test, indicating a lowered crystallinity in CdS (Fig. S2b†). XPS of CdS after hydrogen evolution tests revealed that the S^0 peak at 163.78 eV and the S^{6+} peak at 168.28 eV had formed, indicating the presence of higher-valence sulfur resulting from the oxidation of divalent sulfur (Fig. S2f†). These observations confirm that neat CdS undergoes photocorrosion which likely contributes to its decreasing HER performance over time. In contrast, the HJ exhibits no obvious changes in XRD and XPS patterns after 12 h of HER test, thereby demonstrating its improved stability.

These results suggest there is a cooperative effect between CdS and Ce-UiO-NH$_2$ which contributes to the enhanced photocatalytic activity and stability of the CdS/Ce-UiO-NH$_2$ heterojunctions. The A_{sp} of a catalyst is often correlated to its photocatalytic activity. As MOFs are usually considered as a good catalyst support, we normalized the EQEs to A_{sp} to isolate the influence of A_{sp} on the CdS/Ce-UiO-NH$_2$ heterojunctions' performance. As shown in Table S2,† the corresponding EQE/A_{sp} values for CdS/Ce-UiO-NH$_2$ are larger than those of CdS (0.041 g m^{-2}) when the CdS content is between 30% (0.047 g m^{-2}) and 50% (0.058 g m^{-2}). This indicates that the EQE change of CdS/Ce-UiO-NH$_2$ heterojunction is not only due to the increase of A_{sp} introduced by Ce-UiO-NH$_2$ but also to cooperation between CdS and Ce-UiO-NH$_2$.
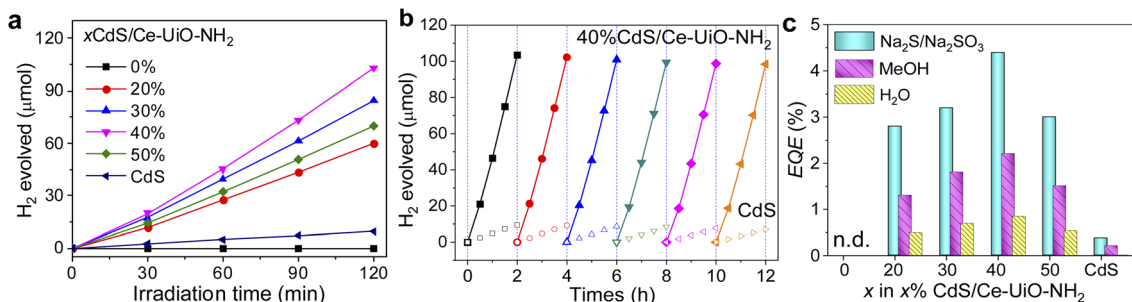
Fig. 2 (a) Photocatalytic evolution of H$_2$ for 25 mg xCdS/Ce-UiO-NH$_2$ in 10 vol% methanol solutions, where x was 0, 20, 30, 40, and 50 wt%, measured for 2 h. (b) 6 sequential 2 h H$_2$ evolution tests for CdS (dotted line) and 40%CdS/Ce-UiO-NH$_2$ (solid line), excited with 420 nm LED lamps in a 10 vol% methanol solution. (c) EQE at 420 nm, measured in 0.35 M Na$_2$S/0.25 M Na$_2$SO$_3$ (unstable), 10 vol% methanol solutions and without sacrificial agents, respectively.

In Fig. 2c, the CdS/Ce-UiO-NH$_2$ heterojunction also shows enhanced HER performance *vs.* neat CdS both in pure water and in the presence of Na$_2$S/Na$_2$SO$_3$. The EQEs follow the same trend with CdS content in all three cases, thereby showing that interaction with the hole scavenger does not explain the EQE trend with CdS content. We note that our previous work showed higher EQE in Na$_2$S/Na$_2$SO$_3$ than in methanol and pure H$_2$O.[21] However, this system was not stable enough for in-depth spectroscopic analysis.

Photophysical characterization

Now, we turn to the photophysical analysis of the origin of the enhanced efficiency of CdS/Ce-UiO-NH$_2$ heterojunctions. 40% CdS/Ce-UiO-NH$_2$, which showed the maximum EQE in H$_2$ evolution, was chosen as the HJ sample for comparison with neat CdS and Ce-UiO-NH$_2$. The PL spectrum was used to gain more insight into electron–hole separation processes in the catalysts (Fig. S1d†). Upon 330 nm excitation, the PL spectrum of CdS showed an intense peak at 550 nm (2.25 eV), which well matches to the band-to-band transition ($E_g = 2.25$ eV), obtained from the optical absorption edge. The PL spectrum of Ce-UiO-NH$_2$ showed a peak centered at 430 nm. The PL spectrum of HJ exhibited two visible peaks centered at 430 and 515 nm. The 515 nm emission peak is attributed to CdS in the HJ, with the

blue-shift relative to pure CdS indicating CdS in the HJ forms smaller particles than pure CdS. Both PL peaks were strongly quenched relative to the neat materials, suggesting that the HJ enables charge separation between CdS and Ce-UiO-NH$_2$. This is in agreement with the enhanced EQE of the HJ for H$_2$ evolution.

We have previously undertaken analyses of the energetics and electrochemistry of neat CdS and UiO-66s, and based on these analyses made preliminarily conclusions on the relative band alignment and direction of charge separation.[21] However, these studies did not include direct measurement of the photogenerated charges. Moreover, the crystallite size reduction of CdS induced by the MOF in the HJ is likely to significantly impact the CdS due to quantum size effects (Fig. 1b and Table S2†). As such, we employ herein both optical transient spectroscopy and spectroelectrochemistry to investigate the underlying charge dynamics and energetics of CdS/Ce-UiO-NH$_2$ HJ photocatalysts.

We first employ transient absorption (TA) spectroscopy to explore the charge transfer mechanism in our CdS/Ce-UiO-NH$_2$ heterojunctions. To achieve efficient HER, the charge carrier lifetimes must be long enough to enable the efficient extraction of holes by methanol and the reduction of protons to molecular H$_2$. Fig. 3 shows the TA spectrum of CdS, Ce-UiO-NH$_2$ and HJ
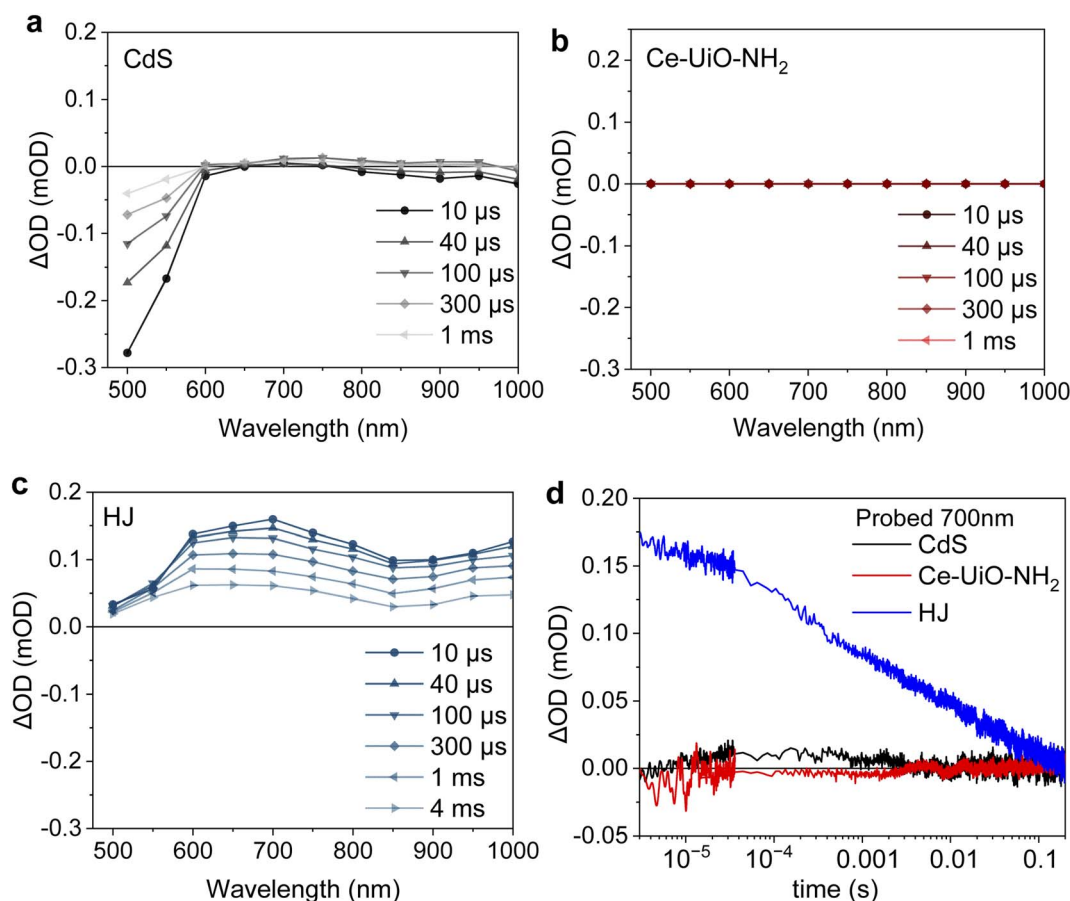

Fig. 3 (a–c) Transient absorption spectra at different time delays, excited at 420 nm (840 μJ cm^{-2}) and (d) decay dynamics of CdS (black), Ce-UiO-NH$_2$ (red) and the HJ (blue) films in water, probed at 700 nm.

films in water on the μs–s timescale under 420 nm excitation. It is notable that the HJ exhibited a broad photoinduced absorption spectrum from 500–1000 nm, with two absorption peaks at 700 nm and 1000 nm. This absorbance has a half-life of 1 ms, which is substantially longer than the half-life of CdS (2 μs) and Ce-UiO-NH$_2$ (sub-μs) alone. The amplitude of the TA kinetic probed at 700 nm was up to 12 times higher for the HJ than for neat CdS and Ce-UiO-NH$_2$, indicating that there is a much higher photogenerated charge density in the HJ on these timescales (Fig. 3d). Interestingly, the trend in photogenerated charge density on the μs timescale (HJ > CdS > Ce-UiO-NH$_2$) matches the trend in HER efficiency of the three materials.

Scavenging tests were further conducted to identify the charge species observed in our TAS data; methanol was used as the hole scavenger, and O$_2$ was used as the electron scavenger. As shown in Fig. S3,† for neat CdS, the bleach probed at 500 nm was partly quenched by O$_2$ and increased by methanol, which indicates this is an electron-dominated signal. The positive absorption signal at 700 nm is quite small and near the resolution limit of our instrument. However, we observed that adding methanol partly quenched this signal, which might suggest it is a hole-dominated signal. The absence of a strong signal from holes in CdS on this microsecond timescale is consistent with reports that trapped holes in CdS have short (ps) lifetimes when measured in ACN.[24–26] For the neat Ce-UiO-NH$_2$, there was negligible TA signal even with the addition of oxygen or methanol, demonstrating that charge recombination in the MOF occurs on the sub-microsecond timescale and is faster than charge transfer to methanol or oxygen. For the HJ, the TA

spectrum from 500–1000 nm was completely quenched on the sub-μs timescale by 10 vol% methanol (Fig. S3c†), indicating that the long-lived TA spectrum of the HJ is a hole-dominated spectra and 10 vol% methanol is able to extract holes from the HJ on sub-μs timescales.

So far, the samples were excited at 420 nm, which excites both CdS and Ce-UiO-NH$_2$. Now we excite at 560 nm, which preferentially excites Ce-UiO-NH$_2$, to investigate whether Ce-UiO-NH$_2$ acts as a light sensitiser or just as a charge separator. The results are shown in Fig. 4. For neat CdS, no TAS signal was observed (Fig. 4a), as expected, because it has no ground state absorption at 560 nm (Fig. 1e). Neat Ce-UiO-NH$_2$ also exhibited no signal (Fig. 4a), which was attributed to rapid charge recombination on the sub-microsecond timescale and is consistent with its TA spectrum under 420 nm excitation (Fig. 3b). However, the TA spectrum of the HJ showed the same broad positive absorbance at 600–1000 nm alongside a negative signal at 500–600 nm (Fig. 4b). These data prove that Ce-UiO-NH$_2$ can act as a light absorber and photogenerate long-lived holes. The 500 nm bleach in the HJ (Fig. 4c) is not observed when exciting at 420 nm (Fig. 3c), possibly because the overlapping positive MOF signal dominates over the negative CdS blench. The bleaching of the CdS ground state in Fig. 4c and the increase in the MOF hole signal in Fig. 4d indicate that in the HJ there is electron transfer from the photoexcited MOF to the unexcited CdS. Overall, these observations based on 560 nm excitation suggest that Ce-UiO-NH$_2$ acts as light absorber and electron donor in our HJ.
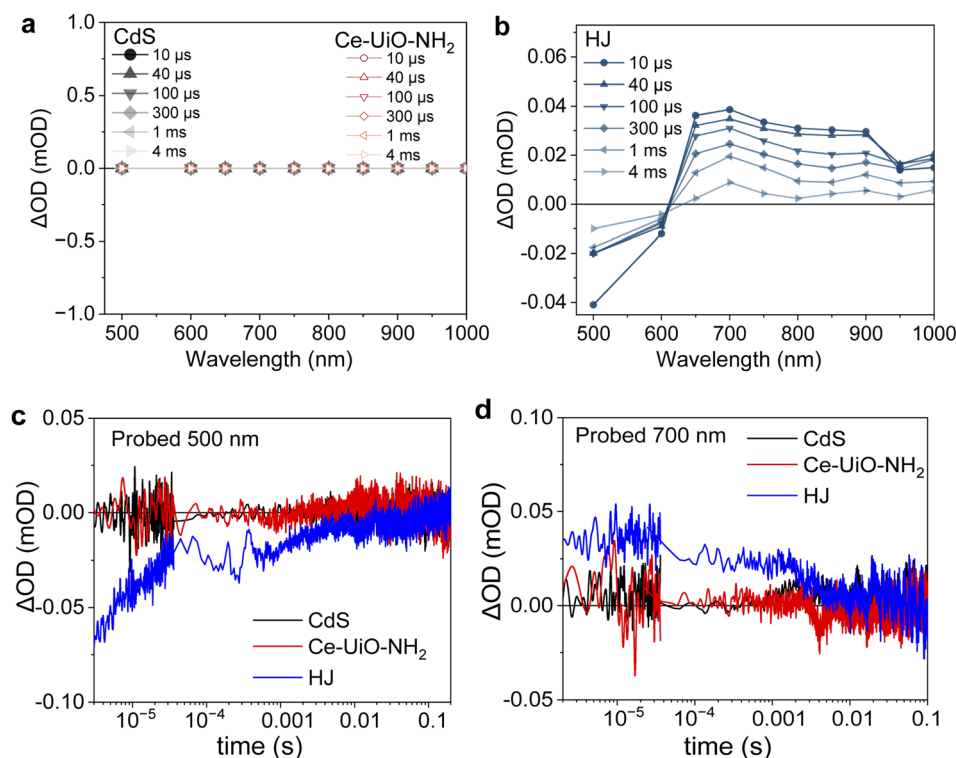

Fig. 4 Transient absorption spectra at different time delays of (a) CdS and Ce-UiO-NH$_2$ and (c) HJ, excited at 560 nm (840 μJ cm^{-2}) and comparison of the decay dynamics of CdS (black), Ce-UiO-NH$_2$ (red) and HJ (blue) films in water, probed at (b) 500 nm and (c) 700 nm.

Our TAS data suggest that the long-lived photoinduced absorption observed for our HJ samples results from Ce-UiO-NH$_2$ holes. To provide further support to this conclusion, spectroelectrochemical measurements (SEC) were conducted to investigate the electron and hole spectra of CdS and Ce-UiO-NH$_2$, respectively. As shown in Fig. 5a, the application of a positive bias to CdS films results in broad bleaching of the absorbance change spectrum, which increases towards the blue visible light region. This bleaching is tentatively assigned to hole formation associated with oxidation of S^{2-} species in CdS, which is one of the origins of CdS self-corrosion and often limits its photocatalytic performance.[24,27] The application of a comparable positive potential to Ce-UiO-NH$_2$ resulted in a broad absorption spectrum across the entire visible spectrum and is assigned to Ce-UiO-NH$_2$ holes. A very similar broad absorption spectrum is observed when positive bias is applied to the HJ (Fig. 5c), suggesting that the Ce-UiO-NH$_2$ is more readily oxidized than the CdS and that oxidation of the HJ happens on the Ce-UiO-NH$_2$. This SEC hole spectrum for Ce-UiO-NH$_2$ (Fig. 5a) is also similar to the hole-dominated signal observed in our HJ TAS measurements (Fig. 3c), confirming our assignment of this TAS HJ signal to the photogeneration of long-lived holes on the Ce-UiO-NH$_2$. For SEC reduction spectra (Fig. 5b and d), the similarity of the SEC spectra measured on CdS and on the HJ suggests that in the HJ, reduction happens more readily on the CdS. The behaviour of the HJ under applied bias, in which oxidation happens on the Ce-UiO-NH$_2$ and reduction happens on the CdS, is consistent with our conclusion that charge separation in our photoexcited HJ results in hole accumulation on the Ce-UiO-NH$_2$ and electron accumulation primarily on the CdS.

Mechanism and discussion

Scheme 1 summarizes the charge separation generated in the optimized HJs determined herein. Our TA studies showed that a much higher yield of long-lived charges survives to the µs–s timescale in the HJ when compared to its individual components. This is strong evidence that the HJ helps generate charges which survive long enough to contribute to HER.[28] TAS measurements were also undertaken using selective Ce-UiO-NH$_2$ excitation, indicating that Ce-UiO-NH$_2$ acts as a light absorber and electron donor. The direction of charge transfer in HJ was further confirmed by SEC. The reduced HJ and reduced CdS SEC spectra have similar shapes, indicating electron accumulation in the HJ primarily occurs on the CdS. On the other hand, the oxidised HJ SEC and oxidised Ce-UiO-NH$_2$ SEC spectra have similar shapes, indicating that hole accumulation in the HJ primarily occurs on the Ce-UiO-NH$_2$. These hole spectra matched the photoexcited TA spectrum of Ce-UiO-NH$_2$ in the presence of methanol, indicating that sub-µs hole extraction by methanol enables hole transfer to, and accumulation on, the MOF.

We note that the direction of charge transfer reported herein is the inverse of that concluded in previous studies of CdS/Zr-UiO-66 and CdS/Zr-UiO-66-NH$_2$ heterojunctions.[17,29,30] This may be the result of Ce-doping facilitating the oxidation of our
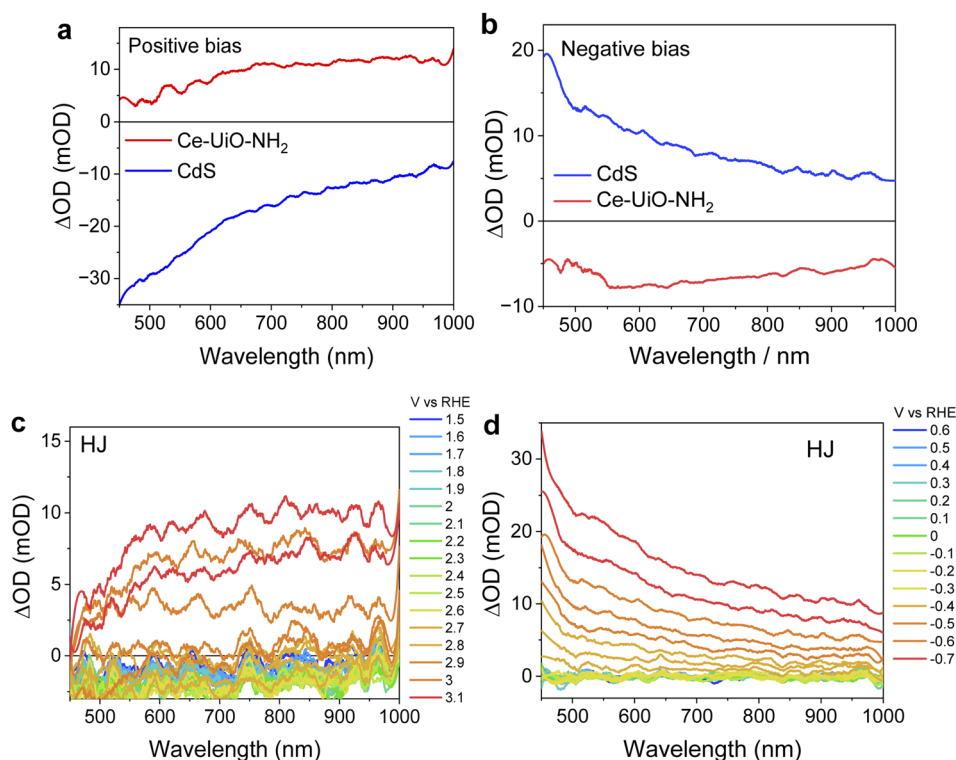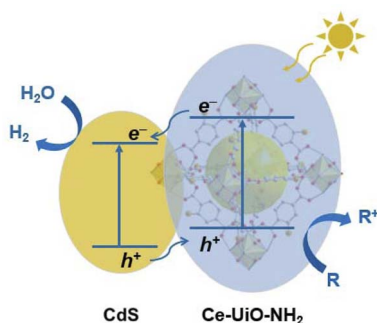

Fig. 5 Absorbance difference spectra at positive bias for (a) CdS and Ce-UiO-NH$_2$, and (c) HJ, respectively and at negative bias for (b) CdS and Ce-UiO-NH$_2$ and (d) HJ, respectively. All films were measured in 0.1 M NaClO$_4$ solution, pH = 7.

Scheme 1 Mechanism of the CdS/Ce-UiO-NH$_2$ heterojunction for enhanced HER in the presence of a sacrificial electron donor 'R'.

MOF.[13,31] It may also result from the different timescales employed for TAS studies. On ultrafast (picosecond) timescales, charge transfer may proceed prior to charge trapping and the direction of transfer is therefore dominated by band edge alignment. On longer (microsecond) timescales, which are likely more relevant to catalysis (e.g.: HER), charges will localize on the most energetically favorable trapping sites within the heterojunction, which may result in a different charge distribution between the two components of the HJ. For the HJ herein, our observation of hole localization on the MOF is particularly advantageous in minimizing CdS corrosion driven by hole accumulation on this material – as evidenced by the high stability of our HJ.

The CdS/Ce-UiO-NH$_2$ heterojunctions employed in this work show a modest EQE of 2.2% for HER. This EQE is limited, at least in part, by the relatively modest light absorption of our photocatalyst suspension. Secondly, the two-step loading most likely results in CdS NPs filling into the pores. Such CdS may be less able to drive HER. It may also decrease the particle size of some of the CdS, shifting their bandgap to >3 eV.[27] Thirdly, in the study herein, no co-catalyst was added for the H$_2$ evolution experiments. For obtaining a higher EQE, adding an established co-catalyst like Pt is an obvious strategy.[32–34] Moreover, alternate sacrificial regents should be explored. Our previous work showed higher EQE in Na$_2$S/Na$_2$SO$_3$ than in methanol, but with a lower stability. Most related photocatalytic HER measurements in the literature have been conducted in either ACN with lactic acid solution; with Na$_2$S/Na$_2$SO$_3$ solution for CdS; or with TEOA for MOFs. However, recent studies indicate that some of these sacrificial regents also cause instability and photocorrosion.[35,36]

Conclusions

In summary, we have reported CdS-loaded Ce-UiO-NH$_2$ heterojunctions for enhanced H$_2$ evolution under visible light in the presence of a methanol hole scavenger. Under visible light, Ce-UiO-NH$_2$ has negligible H$_2$ evolution. The EQE increased from 0 to 2.2% after 40% CdS loading. This HJ EQE was also 11 times higher than neat CdS. To understand the mechanism of this CdS/Ce-UiO-NH$_2$ heterojunction, μs–s TA spectroscopy and spectroelectrochemistry measurements were further

conducted. Firstly, long-lived charges on the millisecond timescale were observed in CdS/Ce-UiO-NH$_2$ heterojunctions, indicating that the heterojunction can achieve effective charge separation. The photogenerated charge density on μs–s timescale follows the order of HJ > CdS > Ce-UiO-NH$_2$, which correlates with their H$_2$ evolution efficiency. Secondly, the specific role of Ce-UiO-NH$_2$ as electron donor in heterojunction was confirmed by preferentially exciting Ce-UiO-NH$_2$. Thirdly, the charge transfer direction was further confirmed by spectroelectrochemical measurements, comprising electron transfer from Ce-UiO-NH$_2$ to CdS, and hole transfer from CdS to Ce-UiO-NH$_2$. The direction of charge transfer is the opposite of recent studies of Zr-UiOs, with hole accumulation on the MOF preventing the corrosion of CdS in HJ. Thus, this work shows the potential of Ce-MOF in photocatalytic HER not only as a driver of charge separation but also as an electron donor, demonstrating that metal node substitution is a promising design strategy for enhanced photoactive MOFs and efficient heterojunctions.

Data availability

The data supporting this article have been included as part of the ESI.†

Author contributions

W. H.: conceptualization, data curation, formal analysis, investigation, methodology, validation, visualization, and writing – original draft. S. A. J. H.: formal analysis, methodology, software, validation, visualization, and writing – review & editing. S. G.-C.: formal analysis, investigation, validation, and visualization. S. Y.: data curation, investigation, and validation. H. Z.: data curation, formal analysis, and resources. J. R. D.: conceptualization, funding acquisition, project administration, resources, supervision, and writing – review & editing.

Conflicts of interest

There are no conflicts to declare.

Acknowledgements

References

1 M. I. Hoffert, K. Caldeira, G. Benford, D. R. Criswell, C. Green, H. Herzog, A. K. Jain, H. S. Kheshgi, K. S. Lackner, J. S. Lewis, H. D. Lightfoot, W. Manheimer, J. C. Mankins, M. E. Mauel, L. J. Perkins, M. E. Schlesinger, T. Volk and T. M. L. Wigley, *Science*, 2002, **298**, 981–987.

2 M. Ball and M. Weeda, *Int. J. Hydrogen Energy*, 2015, **40**, 7903–7919.

3 T. Hisatomi, J. Kubota and K. Domen, *Chem. Soc. Rev.*, 2014, **43**, 7520–7535.

4 B. A. Pinaud, J. D. Benck, L. C. Seitz, A. J. Forman, Z. Chen, T. G. Deutsch, B. D. James, K. N. Baum, G. N. Baum, S. Ardo, H. Wang, E. Miller and T. F. Jaramillo, *Energy Environ. Sci.*, 2013, **6**, 1983–2002.

5 Y.-C. Wang, X.-Y. Liu, X.-X. Wang and M.-S. Cao, *Chem. Eng. J.*, 2021, **419**, 129459.

6 M. A. Syzgantseva, C. P. Ireland, F. M. Ebrahim, B. Smit and O. A. Syzgantseva, *J. Am. Chem. Soc.*, 2019, **141**, 6271–6278.

7 Y. Li, H. Xu, S. Ouyang and J. Ye, *Phys. Chem. Chem. Phys.*, 2016, **18**, 7563–7572.

8 Y. Zhao, J. Wang, W. Zhu, L. Liu and R. Pei, *Nanoscale*, 2021, **13**, 4505–4511.

9 L. Valenzano, B. Civalleri, S. Chavan, S. Bordiga, M. H. Nilsen, S. Jakobsen, K. P. Lillerud and C. Lamberti, *Chem. Mater.*, 2011, **23**, 1700–1718.

10 M. Kandiah, M. H. Nilsen, S. Usseglio, S. Jakobsen, U. Olsbye, M. Tilset, C. Larabi, E. A. Quadrelli, F. Bonino and K. P. Lillerud, *Chem. Mater.*, 2010, **22**, 6632–6640.

11 M. Lammert, M. T. Wharmby, S. Smolders, B. Bueken, A. Lieb, K. A. Lomachenko, D. D. Vos and N. Stock, *Chem. Commun.*, 2015, **51**, 12578–12581.

12 F. A. Son, A. Atilgan, K. B. Idrees, T. Islamoglu and O. K. Farha, *Inorg. Chem. Front.*, 2020, **7**, 984–990.

13 X. P. Wu, L. Gagliardi and D. G. Truhlar, *J. Am. Chem. Soc.*, 2018, **140**, 7904–7912.

14 J. D. Xiao, Q. C. Shang, Y. J. Xiong, Q. Zhang, Y. Luo, S. H. Yu and H. L. Jiang, *Angew. Chem., Int. Ed.*, 2016, **55**, 9389–9393.

15 J. Qiu, X. Zhang, K. Xie, X.-F. Zhang, Y. Feng, M. Jia and J. Yao, *J. Colloid Interface Sci.*, 2019, **538**, 569–577.

16 X. Hou, L. Wu, L. Gu, G. Xu, H. Du and Y. Yuan, *J. Mater. Sci.:Mater. Electron.*, 2019, **30**, 5203–5211.

17 H.-Q. Xu, S. Yang, X. Ma, J. Huang and H.-L. Jiang, *ACS Catal.*, 2018, **8**, 11615–11621.

18 L. Cheng, Q. Xiang, Y. Liao and H. Zhang, *Energy Environ. Sci.*, 2018, **11**, 1362–1391.

19 D. Ayodhya and G. Veerabhadram, *J. Sci.:Adv. Mater. Devices*, 2019, **4**, 381–391.

20 L. J. Shen, M. B. Luo, Y. H. Liu, R. W. Liang, F. F. Jing and L. Wu, *Appl. Catal., B*, 2015, **166**, 445–453.

21 W. Hou, C. Chen, Y. Wang and Y. Xu, *Catal. Sci. Technol.*, 2022, **12**, 4012–4019.

22 J. Kosco, S. Gonzalez-Carrero, C. T. Howells, T. Fei, Y. Dong, R. Sougrat, G. T. Harrison, Y. Firdaus, R. Sheelamanthula, B. Purushothaman, F. Moruzzi, W. Xu, L. Zhao, A. Basu, S. De Wolf, T. D. Anthopoulos, J. R. Durrant and I. McCulloch, *Nat. Energy*, 2022, **7**, 340–351.

23 I. Strauss, K. Chakarova, A. Mundstock, M. Mihaylov, K. Hadjiivanov, N. Guschanski and J. Caro, *Microporous Mesoporous Mater.*, 2020, **302**, 110227.

24 W. Wang, Y. Tao, J. Fan, Z. Yan, H. Shang, D. L. Phillips, M. Chen and G. Li, *Adv. Funct. Mater.*, 2022, **32**, 2201357.

25 Z. Yan, L. Du and D. Lee Phillips, *RSC Adv.*, 2017, **7**, 55993–55999.

26 X. P. Wu, L. Gagliardi and D. G. Truhlar, *J. Chem. Phys.*, 2019, **150**, 041701.

27 S. K. Haram, B. M. Quinn and A. J. Bard, *J. Am. Chem. Soc.*, 2001, **123**, 8860.

28 R. Godin and J. R. Durrant, *Chem. Soc. Rev.*, 2021, **50**, 13372–13409.

29 Z. Lian, Z. Li, F. Wu, Y. Zhong, Y. Liu, W. Wang, J. Zi and W. Yang, *Commun. Chem.*, 2022, **5**, 93.

30 Z. Li, J. Zi, X. Luan, Y. Zhong, M. Qu, Y. Wang and Z. Lian, *Adv. Funct. Mater.*, 2023, **33**, 2303069.

31 P. Parnicka, W. Lisowski, T. Klimczuk, A. Mikolajczyk and A. Zaleska-Medynska, *Appl. Catal., B*, 2022, **310**, 121349.

32 X. Li, W. Bi, L. Zhang, S. Tao, W. Chu, Q. Zhang, Y. Luo, C. Wu and Y. Xie, *Adv. Mater.*, 2016, **28**, 2427–2431.

33 X. Fang, Q. Shang, Y. Wang, L. Jiao, T. Yao, Y. Li, Q. Zhang, Y. Luo and H.-L. Jiang, *Adv. Mater.*, 2018, **30**, 1705112.

34 I. Vamvasakis, B. Liu and G. S. Armatas, *Adv. Funct. Mater.*, 2016, **26**, 8062–8071.

35 Y. Chen, W. Zhong, F. Chen, P. Wang, J. Fan and H. Yu, *J. Mater. Sci. Technol.*, 2022, **121**, 19–27.

36 J. Wang, A. S. Cherevan, C. Hannecart, S. Naghdi, S. P. Nandan, T. Gupta and D. Eder, *Appl. Catal., B*, 2021, **283**, 119626.